Chase, B.F., Kolawole, F., Atekwana, E.A., Carpenter, B.M., Turko, M., Abdelsalam, M., and Finn, C., 2022, The 180-km-long Meers-Willow Fault System in the Southern Oklahoma Aulacogen: A potential U.S. mid-continent seismic hazard: GSA Bulletin, https://doi.org/10.1130/B36363.1.

Supplemental Material

AEROMAGNETIC DATA PROCESSING

All magnetic processing was done in Geosoft's Oasis Montaj software suite using industry standard techniques provided in the software package. All grids are displayed with the color default hill shade. Surveys, data links, and key data details can be found in Table S1 below.

The more in-depth aeromagnetic processing is as follows:

Subsets (known as 'masks') of the North American Magnetic Anomaly map (NAMAM) map, which is largely National Uranium Resource Evaluation (NURE) data in Oklahoma and Texas, were taken to examine the South Central United States (Oklahoma and Texas) anomalies.

All data were then Reduced-to-Pole (RTP) in order to center anomalies over their causative bodies, and to allow easier correlation of anomalies with geologic information (Baranov, 1957; Baranov and Naudy, 1964; Arkani-Hamed, 1988). RTP filtering values of declination and inclination were taken on the dates below. Note that these dates represent the approximate calendar day midpoint for the surveys. In the case of the NAMAM/NURE data, the date is the rough midpoint of the individual survey blocks that constitute the regional magnetic data:

Dates are in decimal years.
NAMAM/NURE: 1976.421
2017: 2017.721
1954: 1954.833

The 1954 data was then masked to keep effects of knitting with the newer, higher quality, 2017 data to a minimum. In practice this meant that the 1954 data coverage was reduced to a minimum that would fill gaps in the 2017 data while also maximizing solo coverage of the 2017 data. This was done primarily because the 1954 data has sparse to no original survey documentation, as noted by Sweeney and Hill (2005), and only a final magnetic anomaly value labeled 'mag_anom' is provided. Similar to what has been noted in NURE data lacking documentation (see Hill et al., 2009), we assume that this represents some processed magnetic value with an undetermined International Geomagnetic Reference Field (IGRF) having been removed in the past. Because a lack of documentation means that the processing cannot be undone, we were left with large nanotesla (nT) value discrepancies between the 2017 and 1954 data when measured at any overlapping point, even though grids displayed similar anomalies over the overlapping regions. As a result, we opted to mask as much of the 1954 data as possible to limit its influence on final maps.

Grid merging or 'knitting' two grids directly together is a standard process in Oasis Montaj, but given the limited information regarding the 1954 data set we modified this knitting method by first leveling the 1954 and 2017 data relative to the NAMAM/NURE data. The result is a knitted grid that has had its independent sub-grids, in this case the 2017 and 1954 grids, leveled about a constant value provided by the regional grid (Oasis Montaj support, personnel communication). After some visual comparisons using grids produced by alternative knitting processes we deemed this process to be the best at maintaining structures unique to each data set, while also providing the most seamless knitting of the grids (i.e., less knitting artifacts) over regions where the individual-grids overlapped. We then knitted this grid to the NAMAM/NURE data. Individual parameters in the knitting process were left on default settings, as various knitting renditions where these parameters were changed proved to produce limited to no improvements.

To assess the subsurface extent of key features the data was processed using matched bandpass filtering, which separates potential-field data into anomaly components representing different source depths. The implementation of the filtering was applied to the merged, reduced to the pole magnetic data using a GX in Oasis Montaj based on a USGS software package (Phillips, 1997). Matched filtering is accomplished in three steps. The initialization program first prepares the input data grid for Fourier transform by extending the rows and columns and then computes the Fourier transform and the natural logarithms of the radially-symmetric part (RSP) of the Fourier power spectrum and the non-radially symmetric part of the power spectrum. The matched bandpass filters are designed interactively by fitting equivalent source layers to the log of RSP power and also nonlinearly adjusts the equivalent layer parameters to better fit the observed spectrum. The actual bandpass filtering calculates the inverse Fourier transforms and removes the row and column extensions (Phillips, 2001). The RSP of the power spectrum of the magnetic data was matched by a four-layer equivalent model, consisting of three shallow equivalent dipole layers (corresponding to depths of 38 m, 432 m and 1576 m and a single deep equivalent magnetic half space (6522 m depth). The four corresponding bandpass filters were applied to the data. The results of applying bandpass filters 1–3 to the data are shown in Figure S2. The layer at 38 m (not shown in Fig. S2) was not used in the analysis because it primarily contained very short-wavelength, low-amplitude noise.

Outside of the matched bandpass filtering the grid was upward continued by 400 m in order to remove shorter wavelength features (Jacobsen, 1987) related to cultural noise from regional oil and gas infrastructure (e.g., transcontinental pipelines and well pads), so as to aid structural interpretation. 400 m was selected by trial-and-error on the basis of trying to find an upward continuation elevation which removed obvious cultural noise while still maintaining data resolution so that digitization of longer linear magnetic gradients was not impacted. Post upward continuation, the grids then had the first vertical derivative taken. The first vertical derivative measures the vertical rate of change in total magnetic intensity (i.e., residual) data and is used to better detect and illustrate the edges of magnetized bodies (Nabighian et al., 2005; Kinabo et al., 2008, 2007; Kolawole et al., 2018). Vertical derivatives also tend to make anthropogenic noise and knitting artifacts more obvious, and is another reason why the data was upward continued by 400 m.

NOTES ON EACH AEROMAGNETIC DATASET

2017 data

Further details as well as a full contractors report containing survey can be found at the link provided in Table S1.

1954 data

Survey data and secondary processing performed by Sweeney and Hill (2005) can be found in the link provided in Table S1.

NAMAM/NURE data

The NAMAM data set is a compilation of existing data sets across the United States, and is available for download in the link in Table S1. Frequently, as in the region of this survey, the NURE data set is all that is available. However, in many other regions higher resolution surveys are available, which may have had their resolutions artificially lowered by various processing steps in order to more seamlessly knit these higher-resolution surveys to adjacent lower resolution surveys (see Bankey et al., 2002). The opposite may also be true, where lower resolution data sets may have their resolution artificially increased to fit the average value of the NAMAM data set. Interested users are advise to read the metadata for the national map and individual surveys, as simply sub-setting (masking) the national map, as was done here, can potentially mean working with lower resolution data than is actually available in any single region.

If a user is more interested in working with individual NURE blocks they are referred to Hill et al. (2009) and the associated webpage in Table S1, which acts as the portal for the individual NURE blocks by U.S. state.

DEPTH TO BASEMENT DATA AND METHODS

Many well logs used are the proprietary property of IHS Markit, others are supplemented from Oklahoma Geological Survey (OGS) logs, which are publicly available below.

The map was hand contoured in GeoGraphix using well data and surface exposures of basement. The top of basement was picked on well logs when intercepted. If not, the top of basement was projected to be deeper than the total depth of any single well. Aeromagnetic, 2D seismic, and tops from wells logs were used to constrain fault geometries. En-echelon faults in the south-west part of the map were modified from Heran et al. (2003). This map only extends over the parts of the Wichita Uplift where the well data is most available (Fig. S1).

OGS well data may be found here:

http://www.ou.edu/ogs/data/oil-gas–Under “Wells Drilled to Basement” – Table 1 XLS

A summary of the methodology that went into developing this OGS compilation may be found here:

http://ogs.ou.edu/docs/specialpublications/SP2006-1.pdf

SEISMIC DATA

Seismic data is controlled by Chesapeake Energy and Seismic Exchange Inc. (SEI). Uninterpreted sections may be found in Fig. S4.

FIELD DATA AND METHODS

At the field location, we document the meso-scale brittle (fractures) and ductile (folding) structural deformation of the outcropping units (Fig. 5). To better understand the dominant trends of the fractures, we compliment the outcrop observations with the mapping of fractures from high resolution (~0.25 m spatial resolution) Google Earth© satellite images, which provide a wider coverage of the outcrops.

REMOTE SENSING DATA AND METHODS

Examination of regional fracture by satellite image mapping is a standard practice (e.g., Kolawole et al., 2019). Considering the limited resolution of the seismic and aeromagnetic data and non-uniqueness of geophysical data, we perfume this exercise to provide another line of data on the structural trends in the Wichita Uplift. We manually map the fractures using satellite images from the Google Earth© program and analyze them for systematic organization. They do show such systematic organization (Fig. 6A, C), and locally occur as long deeply incised rectilinear valleys when in the field. These rectilinear valleys are a typical representation of penetrative basement-rooted fracture zones in areas of shallowly buried or exposed crystalline basement (e.g., Drury, 2001). The fracture data was collected at an eye altitude of 60 km. This altitude was chosen as it represented the elevation where both smaller scale fractures and features associated with unroofing were removed from the visual field while maintaining a sufficient number of measurement points so that trends of the larger fractures could be established.

To support this data we took and reproduced data from McLean and Stearns (1986), who embarked on a systematic field study of fractures and faults in the Wichita Granites (Wichita Mountains) (Fig. 6C). The fault zones they map were determined from aerial photographs and their kinematics are constrained by field observations of local reidel-pattern fractures, and offsets of quartz veins and mafic dikes at a single location within each of the fault zones (McLean and Stearns, 1986).

ANALYSIS OF SEISMIC HAZARD POTENTIAL METHODS

Previous studies of Precambrian crystalline basement faults in Oklahoma and their seismicity provided constraints on the mechanical parameters of the faults (Table S2). A primary parameter is the regional maximum compressive principal stress direction (SHmax) of ~N85°E, that is typically cited for Oklahoma, and which is the stress magnitude found at ~5 km depth in the basement (Alt and Zoback, 2017). Other parameters are the rock cohesion, the coefficients of static friction for both intact crystalline basement rocks and those with pre-existing weaknesses (Katz et al., 2001; Kolawole et al., 2019), and the geometrical parameters of the faults under consideration (Table S2).

Given that each fault can be hosted in a variety of basement units we slightly alter the rock friction coefficient for those with pre-existing weaknesses to reflect the mean value for a compilation of basement units in Oklahoma (Kolawole et al., 2019). Other parameters such as stress magnitudes are not altered as these data are more relevant for assessing specific faults of interest, and the effects of these parameters on the probability of fault slip are generally more predictable (e.g., greater stress magnitude results in more faults meeting failure conditions).

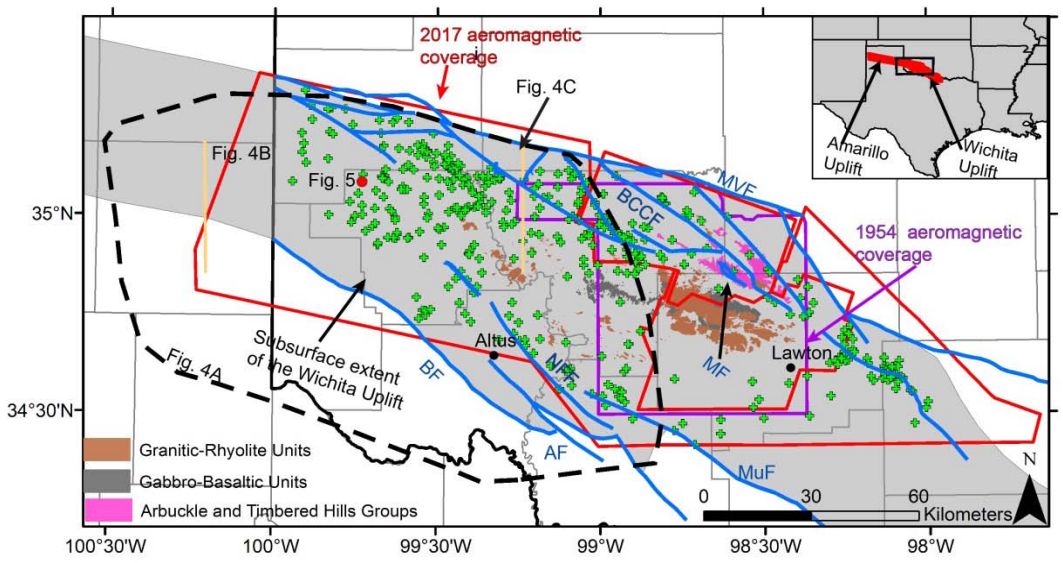

Figure S1. Map of the Wichita Uplift section of the Southern Oklahoma Aulacogen and data coverages. The red dot is the field location studied in Figure 5. Geologic units and the subsurface extent of the Wichita Uplift are modified from maps produced by the Oklahoma Geologic Survey. Green crosses indicate well locations used to make Figure 4A. Blue lines are faults from Marsh and Holland (2016) and are MVF-Mountain View Fault; BCCF-Blue Creek Canyon Fault; MF-Meers Fault; NFF- North Fork Fault; BF-Burch Fault; MuF-Muenster Fault; AF-Altus Fault.

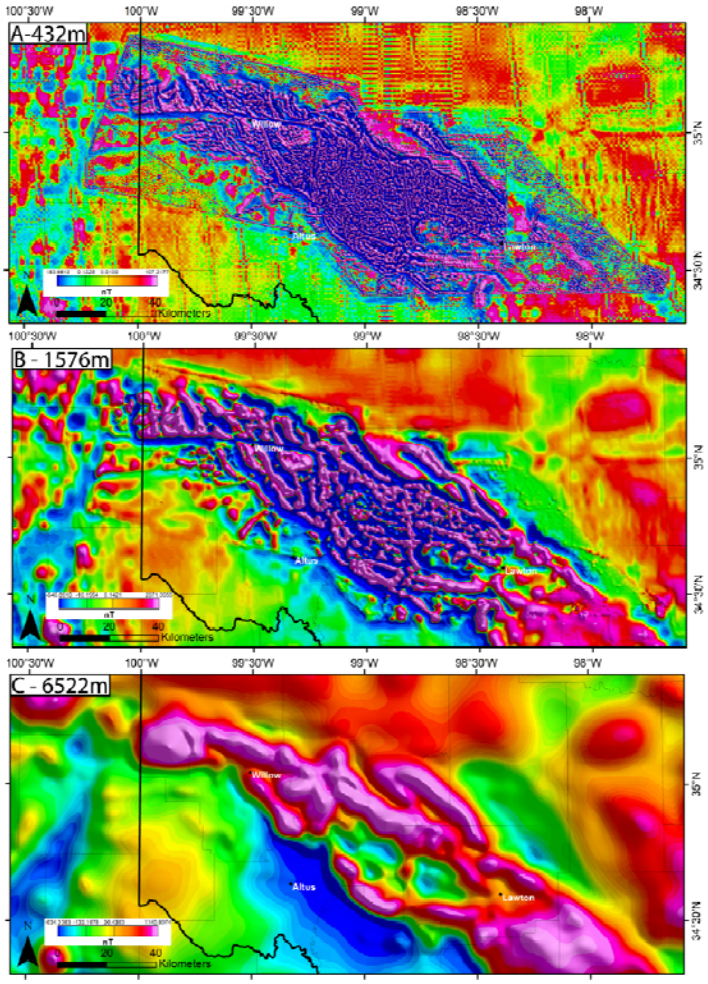

Figure S2. Matched bandpass filtering images showing magnetic anomalies below (A) 432 m, (B) 1576 m, and (C) 6522 m.

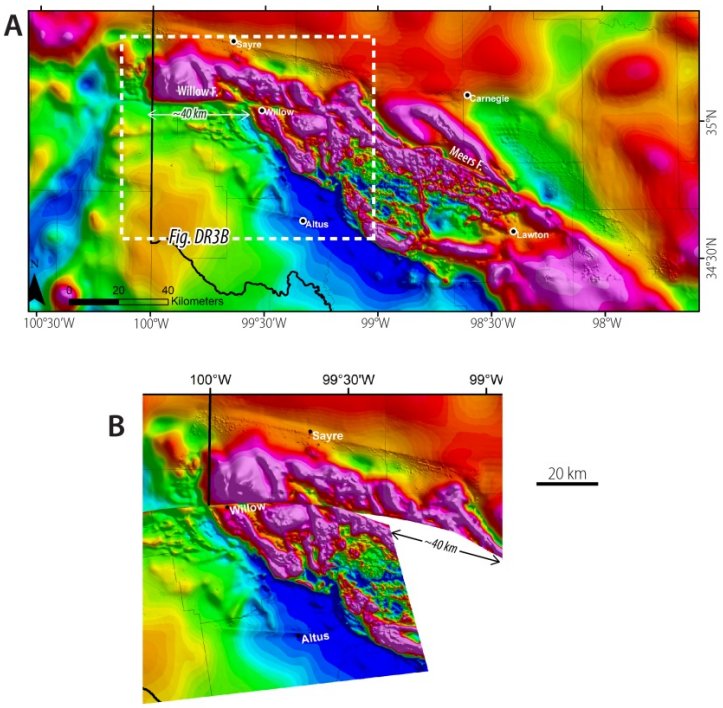

Figure S3. (A) Reduced-to-Pole magnetic map highlighting the displacement along the Willow Fault. (B) A possible reconstruction of the magnetic basement pre-displacement by the Willow Fault.

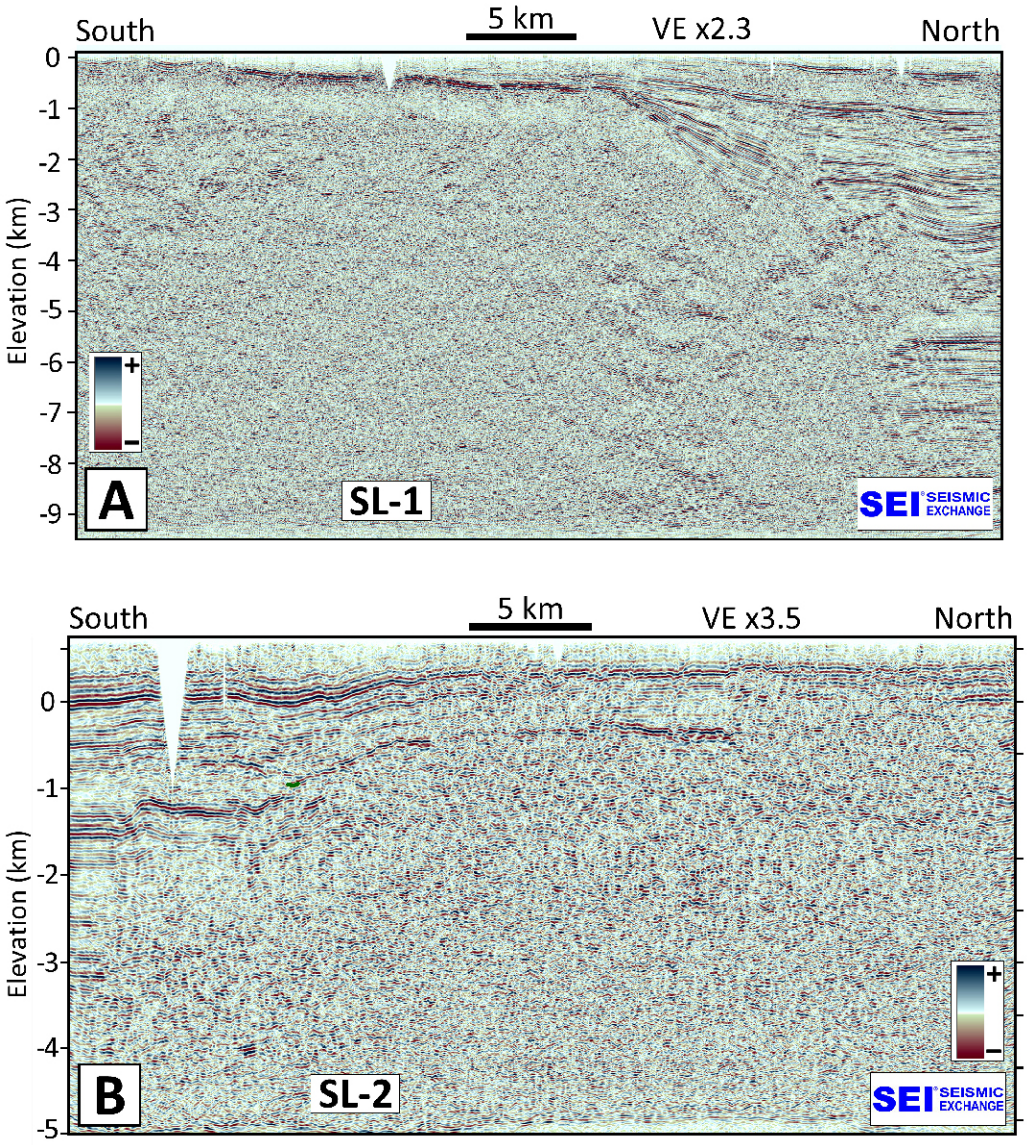

Figure S4. (A) Uninterpreted western seismic section SL-1. (B) Uninterpreted seismic section Sl-2.

Survey Year/Name, Citation	Data Website	Flight height (m) / Line Spacing (m) / Flight direction / Tie line spacing / Tie line direction (m)
2017 Shah and Finn (2018)	https://doi.org/10.5066/F7ZG6RJP	138 / 400 with 200 infill / NE-SW / 4000 / E-W
1954 Sweeney and Hill (2005)	https://doi.org/10.3133/ds138 Click "Get Data"	152 / 402 / E-W / unknown
1974–1981 – "NURE" Variety of years - "National Magnetic Anomaly Map of North America" or "NAMAM" Hill et al. (2009)	https://doi.org/10.3133/ofr20091129 For Individual NURE Grids https://doi.org/10.3133/ofr02414 For the United States national grid and individual surveys (NAMAM)	-121 / ~4800 / E-W / single cross continental tie line

Table S1. Details for the aeromagnetic data used in this survey.

Parameter	Mean Value	Notes
Stress State	N/A	Strike-slip state is determined from A_phi in Lund Snee and Zoback (2016)
Coefficient of friction (intact rock)	1.31	Mount Scott Granite (Wichita Uplift, Southern Oklahoma) from Katz et al. (2001)
Cohesion (intact rock)	46 MPa	Mount Scott Granite (Wichita Uplift, Southern Oklahoma) from Katz et al. (2001)
SHmax	155.42 MPa	Mean SHmax magnitude at 5km depth for Oklahoma, from Walsh and Zoback (2016)
SHmin	76.6 MPa	Mean SHmin magnitude at 5km depth for Oklahoma, from Walsh and Zoback (2016)
SHmax orientation	085° or 69°	Mean SHmax for Oklahoma and near the SOA at 5–6 km depth, respectively, from Alt and Zoback (2017)
Pore pressure	47.5 MPa	Natural pore pressure distribution of 45.2–50.9 MPa bounds (Nelson et al., 2015; Walsh and Zoback, 2016). Mean estimate is for 5 km depth.
Coefficient of friction (pre-existing Basement Fault)	0.68 or .664 (for FPS)	First value is for granite basement faults from Oklahoma, second value is the mean coefficient for faults in a variety of basement units found in Oklahoma. Data from Kolawole et al. (2019) and Lockner et al. (2019).
Meers Fault Geometry:		
Strike	300°	Surface trace and aeromagnetic data (this study)
Dip	89°	From Jones-Cecil (1995); dip of steep Oklahoma basement faults in Walsh and Zoback (2016)
Willow Fault Geometry:		
Strike	91°	Aeromagnetic data and mean trend of surface deformation (this study)
Dip	89°	From Jones-Cecil (1995); dip of steep Oklahoma basement faults in Walsh and Zoback (2016)

Table S2. Parameter values used for the Mohr-Coulomb Failure and Fault Slip Potential analyses of Oklahoma basement faults.

REFERENCES CITED

Alt, R.C., and Zoback, M.D., 2017, In Situ Stress and Active Faulting in Oklahoma: Bulletin of the Seismological Society of America, v. 107, p. 216–228, https://doi.org/10.1785/0120160156.

Arkani-Hamed, J., 1988, Differential reduction-to-the-pole of regional magnetic anomalies: Geophysics, v. 53, p. 1592–1600, https://doi.org/10.1190/1.1442441.

Bankey, V., et al., 2002, Digital data grids for the magnetic anomaly map of North America: U.S. Geological Survey Open-File Report 02-414, https://doi.org/10.3133/ofr02414.

Baranov, V., and Naudy, H., 1964, Numerical calculation of the formula of reduction to the magnetic pole: Geophysics, v. 29, p. 67–79, https://doi.org/10.1190/1.1439334.

Baranov, V., 1957, A new method for interpretation of aeromagnetic maps: pseudo-gravimetric anomalies: Geophysics, v. 22, p. 359–382, https://doi.org/10.1190/1.1438369.

Drury, S.A., 2001, Image interpretation in geology, 3rd Edition: UK, Nelson Thornes Ltd, 304 p.

Heran, W.D., Green, G.N., and Stoeser, D.B., 2003, A Digital Geologic Map Database for the State of Oklahoma: U.S. Geological Survey Open-File Report 2003-247, p. 2003–2247, https://doi.org/10.3133/ofr03247.

Hill, P.L., Kucks, R.P., and Ravat, D., 2009, Aeromagnetic and aeroradiometric data for the conterminous United States and Alaska from the National Uranium Resources Evaluation (NURE) Program of the U.S. Department of Energy: U.S. Geological Survey Open-File Report 2009-1129, p. 2009–1129, https://doi.org/10.3133/ofr20091129.

Jacobsen, B.H., 1987, A case for upward continuation as a standard separation filter for potential-field maps: Geophysics, v. 52, p. 1138–1148, https://doi.org/10.1190/1.1442378.

Jones-Cecil, M., 1995, Structural controls of Holocene reactivation of the Meers fault, southwestern Oklahoma, from magnetic studies: Geological Society of America Bulletin, v. 107, p. 98–112, https://doi.org/10.1130/0016-7606(1995)107<0098:SCOHRO>2.3.CO;2.

Katz, O., Gilbert, M.C., Reches, Z., and Roegiers, J.C., 2001, Mechanical properties of Mount Scott granite, Wichita Mountains, Oklahoma: Oklahoma Geology Notes, v. 61, p. 28–34.

Kinabo, B.D., Atekwana, E.A., Hogan, J.P., Modisi, M.P., Wheaton, D.D., and Kampunzu, A.B., 2007, Early structural development of the Okavango rift zone, NW Botswana: Journal of African Earth Sciences, v. 48, p. 125–136, https://doi.org/10.1016/j.jafrearsci.2007.02.005.

Kinabo, B.D., Hogan, J.P., Atekwana, E.A., Abdelsalam, M.G., and Modisi, M.P., 2008, Fault growth and propagation during incipient continental rifting: Insights from a combined aeromagnetic and Shuttle Radar Topography Mission digital elevation model investigation of the Okavango Rift Zone, northwest Botswana: Tectonics, v. 27, TC3013, https://doi.org/10.1029/2007TC002154.

Kolawole, F., Atekwana, E.A., Laó-Dávila, D.A., Abdelsalam, M.G., Chindandali, P.R., Salima, J., and Kalindekafe, L., 2018, High-resolution electrical resistivity and aeromagnetic imaging reveal the causative fault of the 2009 M w 6.0 Karonga, Malawi earthquake: Geophysical Journal International, v. 213, p. 1412–1425, https://doi.org/10.1093/gji/ggy066.

Kolawole, F., Johnston, C.S., Morgan, C.B., Chang, J.C., Marfurt, K.J., Lockner, D.A., Reches, Z., and Carpenter, B.M., 2019, The susceptibility of Oklahoma's basement to seismic reactivation: Nature Geoscience, v. 12, p. 839–844, https://doi.org/10.1038/s41561-019-0440-5.

Lockner, D.A., Kolawole, F., Chang, J.C., and Carpenter, B.M., 2019, Data release for the susceptibility of Oklahoma's basement to seismic reactivation published in NGEO 2019: U.S. Geological Survey data release, https://doi.org/10.5066/P9AJWOZD.

Marsh, S., and Holland, A., 2016, Comprehensive fault database and interpretive fault map of Oklahoma: Oklahoma Geological Survey Open-File Report OF2-2016, 15 p.

McLean, T.R., and Stearns, D.W., 1986, Stop 7: Hale spring locality. Petrology of the Cambrian Wichita Mountains Igneous Suite: Oklahoma Geological Survey: Guidebook, v. 23, p. 172–178.

Nabighian, M.N., Grauch, V.J.S., Hansen, R.O., LaFehr, T.R., Li, Y., Peirce, J.W., Phillips, J.D., and Ruder, M.E., 2005, The historical development of the magnetic method in exploration: Geophysics, v. 70, no. 6, p. 33ND–61ND, https://doi.org/10.1190/1.2133784.

Nelson, J.D., Chao, K.C., Overton, D.D., and Nelson, E.J., 2015, Foundation engineering for expansive soils, 416 p, https://doi.org/10.1002/9781118996096.

Phillips, J., 1997, Potential-field geophysical software for the PC, version 2.2: U.S. Geological Survey Open-File Report 97-725, p. 97–725, https://doi.org/10.3133/ofr97725.

Phillips, J.D., 2001, Designing matched bandpass and azimuthal filters for the separation of potential-field anomalies by source region and source type: ASEG Extended Abstracts, v. 2001, p. 1–4, https://doi.org/10.1071/ASEG2001ab110.

Shah, A.K., and Finn, C.A., 2018, Airborne Magnetic Surveys over Oklahoma, 2017: U.S. Geological Survey data release, https://doi.org/10.5066/F7ZG6RJP.

Snee, J.E.L., and Zoback, M.D., 2016, State of stress in Texas: Implications for induced seismicity: Geophysical Research Letters, v. 43, p. 10,208–10,214, https://doi.org/10.1002/2016GL070974.

Sweeney, R.E., and Hill, P.L., 2005, Nebraska, Kansas, and Oklahoma aeromagnetic and gravity maps and data: a web site for distribution of data: U.S. Geological Survey Data Series, v. 138, https://doi.org/10.3133/ds138.

Walsh, F.R., III, and Zoback, M.D., 2016, Probabilistic assessment of potential fault slip related to injection-induced earthquakes: Application to north-central Oklahoma, USA: Geology, v. 44, p. 991–994, https://doi.org/10.1130/G38275.1.

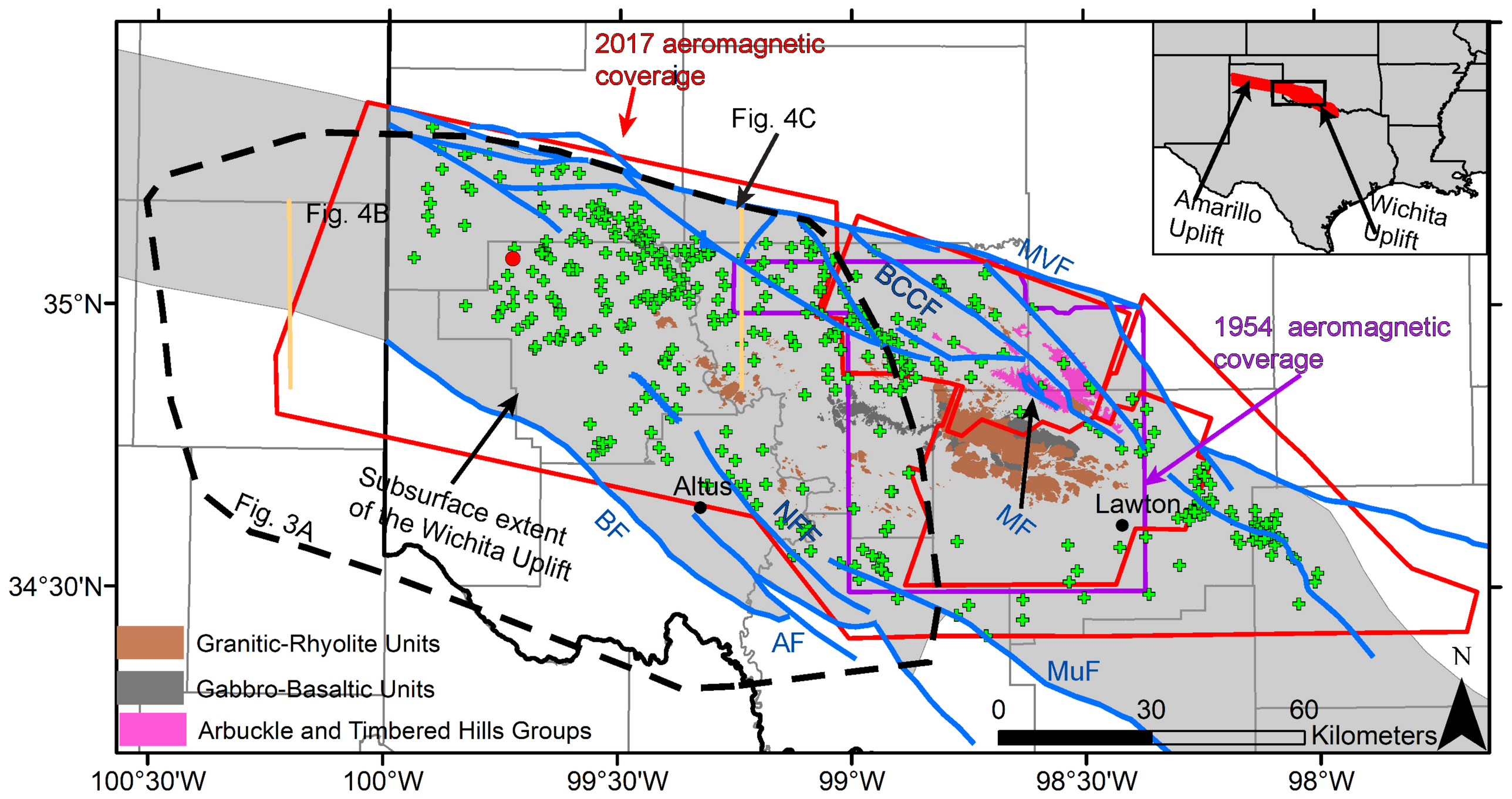
2017 aeromagnetic coverage
Fig. 4C
Fig. 4B
Fig. 3A
Subsurface extent of the Wichita Uplift
1954 aeromagnetic coverage
Amarillo Uplift
Wichita Uplift
MVF
BCCF
MF
NF
BF
AF
MuF
Altus
Lawton
35°N
34°30'N
100°30'W
100°W
99°30'W
99°W
98°30'W
98°W
Granitic-Rhyolite Units
Gabbro-Basaltic Units
Arbuckle and Timbered Hills Groups
0
30
60
Kilometers
N

100°30'W 100°W 99°30'W 99°W 98°30'W 98°W

A-432m

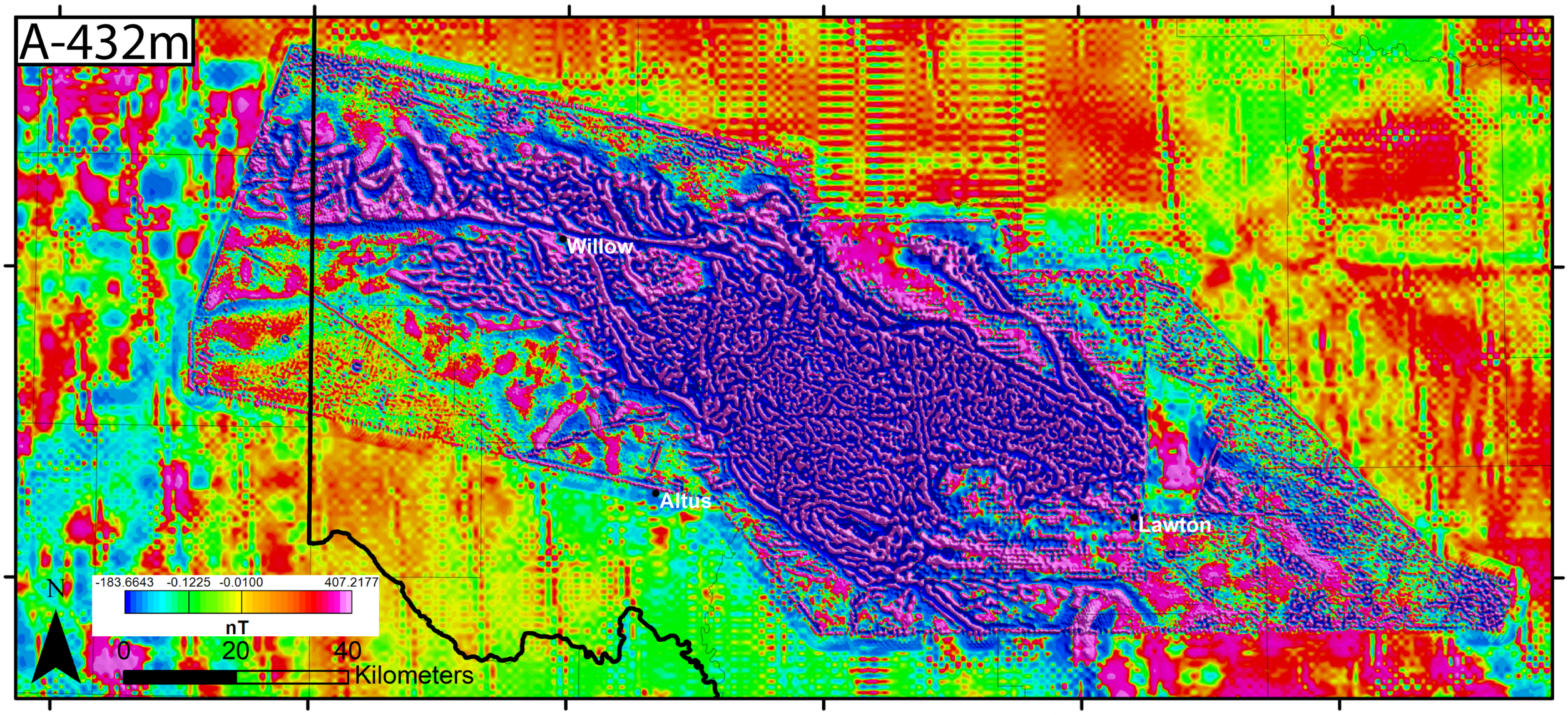

35°N 34°30'N

100°30'W 100°W 99°30'W 99°W 98°30'W 98°W

B - 1576m

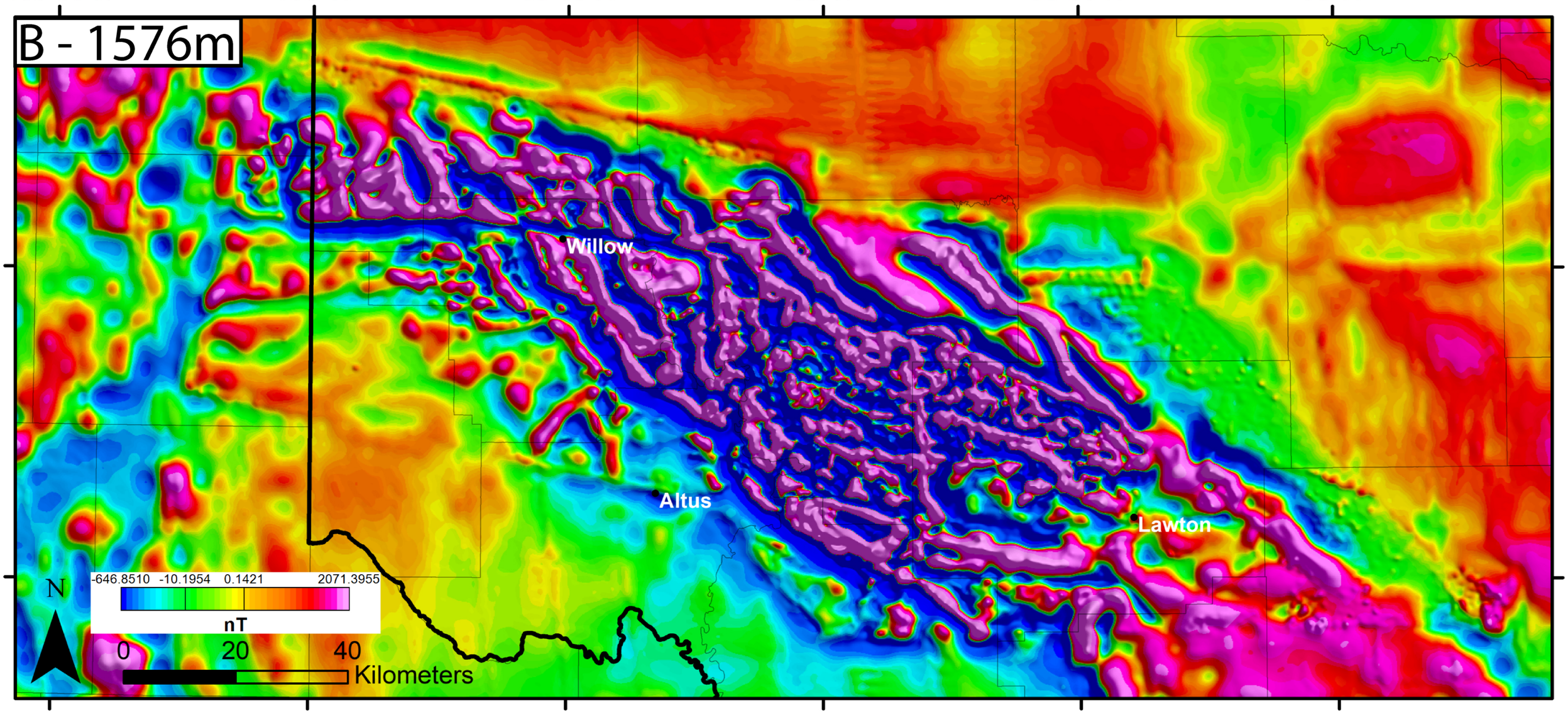

35°N 34°30'N

100°30'W 100°W 99°30'W 99°W 98°30'W 98°W

C - 6522m

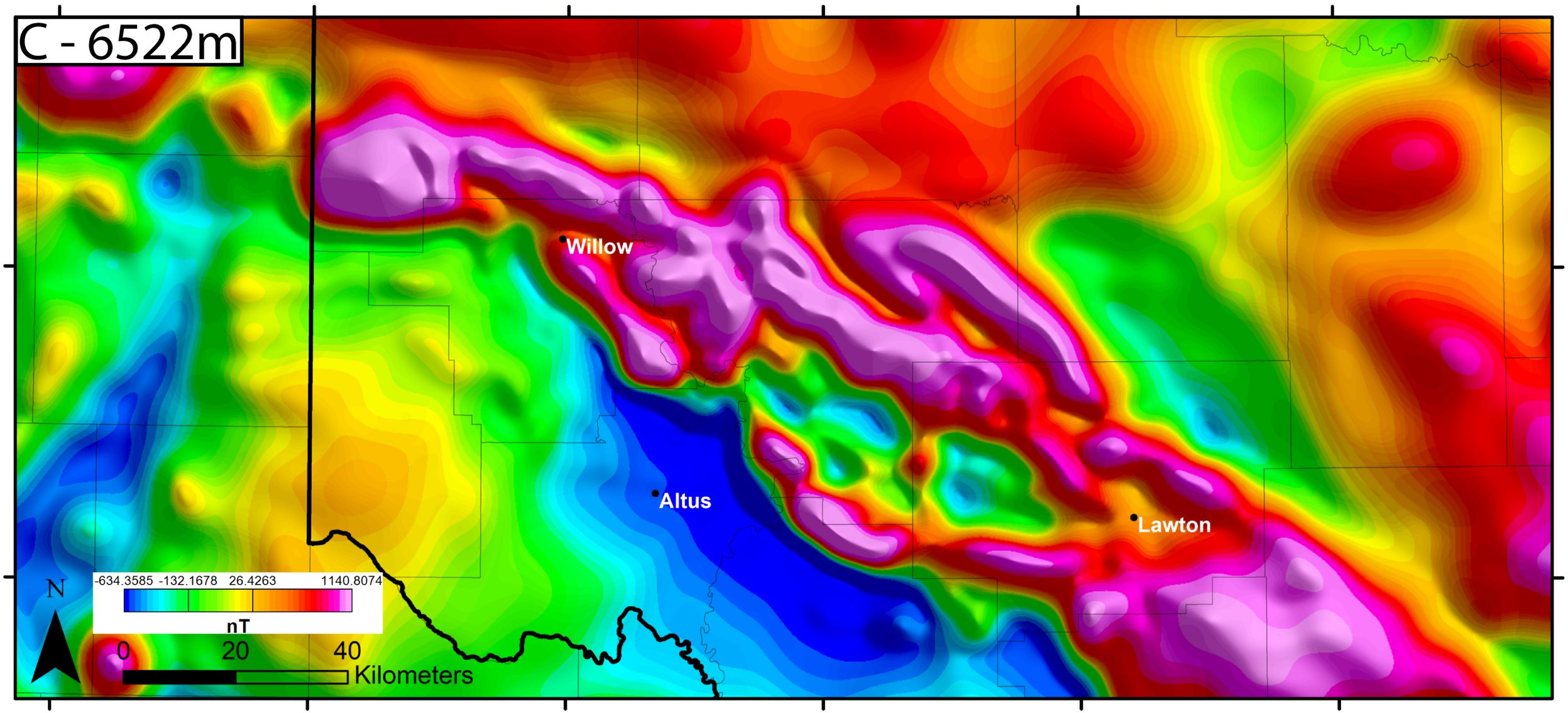

35°N 34°30'N

A

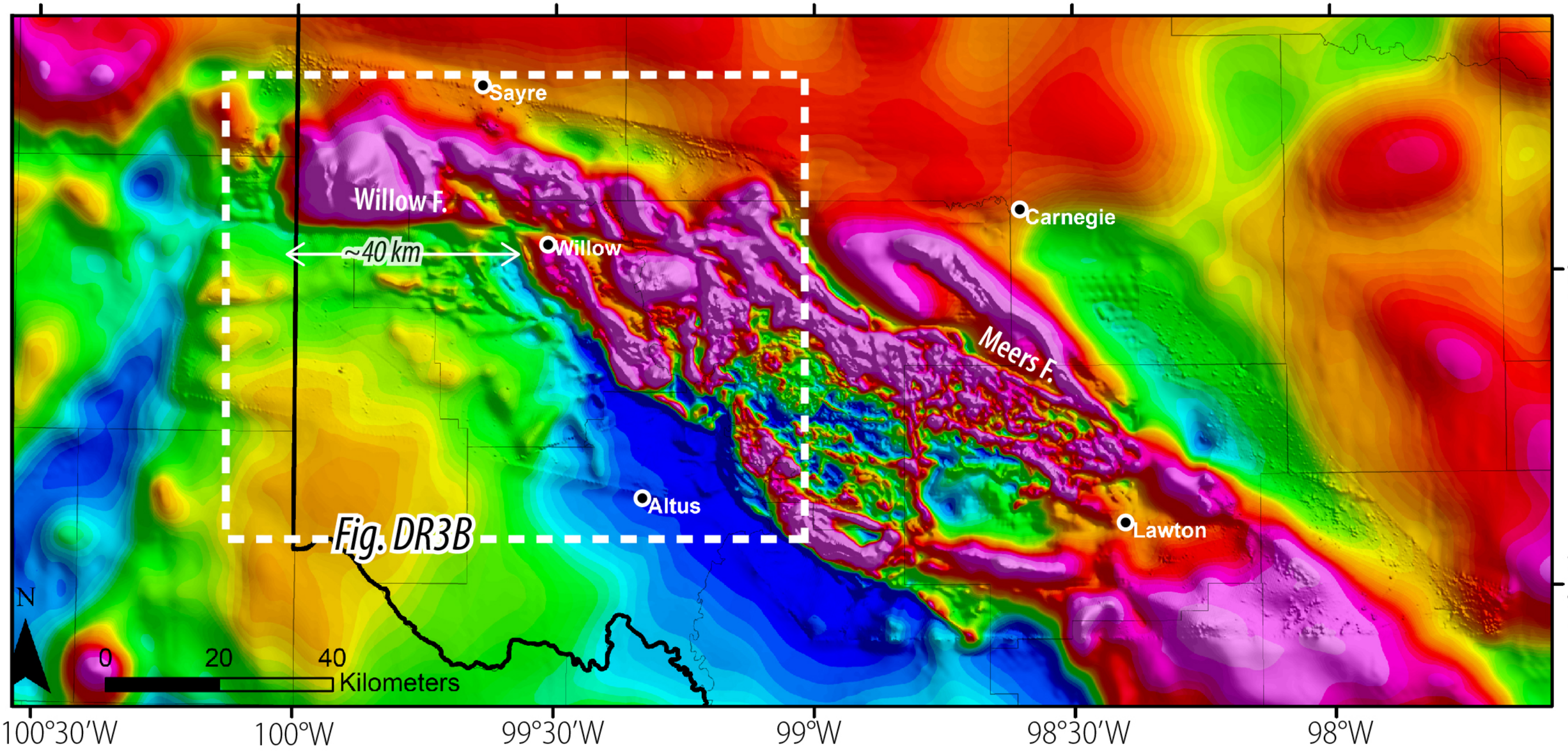
Sayre
Willow F.
~40 km
Willow
Carnegie
Meers F.
Altus
Lawton
Fig. DR3B
N
0
20
40
Kilometers
100°30'W
100°W
99°30'W
99°W
98°30'W
98°W
35°N
34°30'N

B

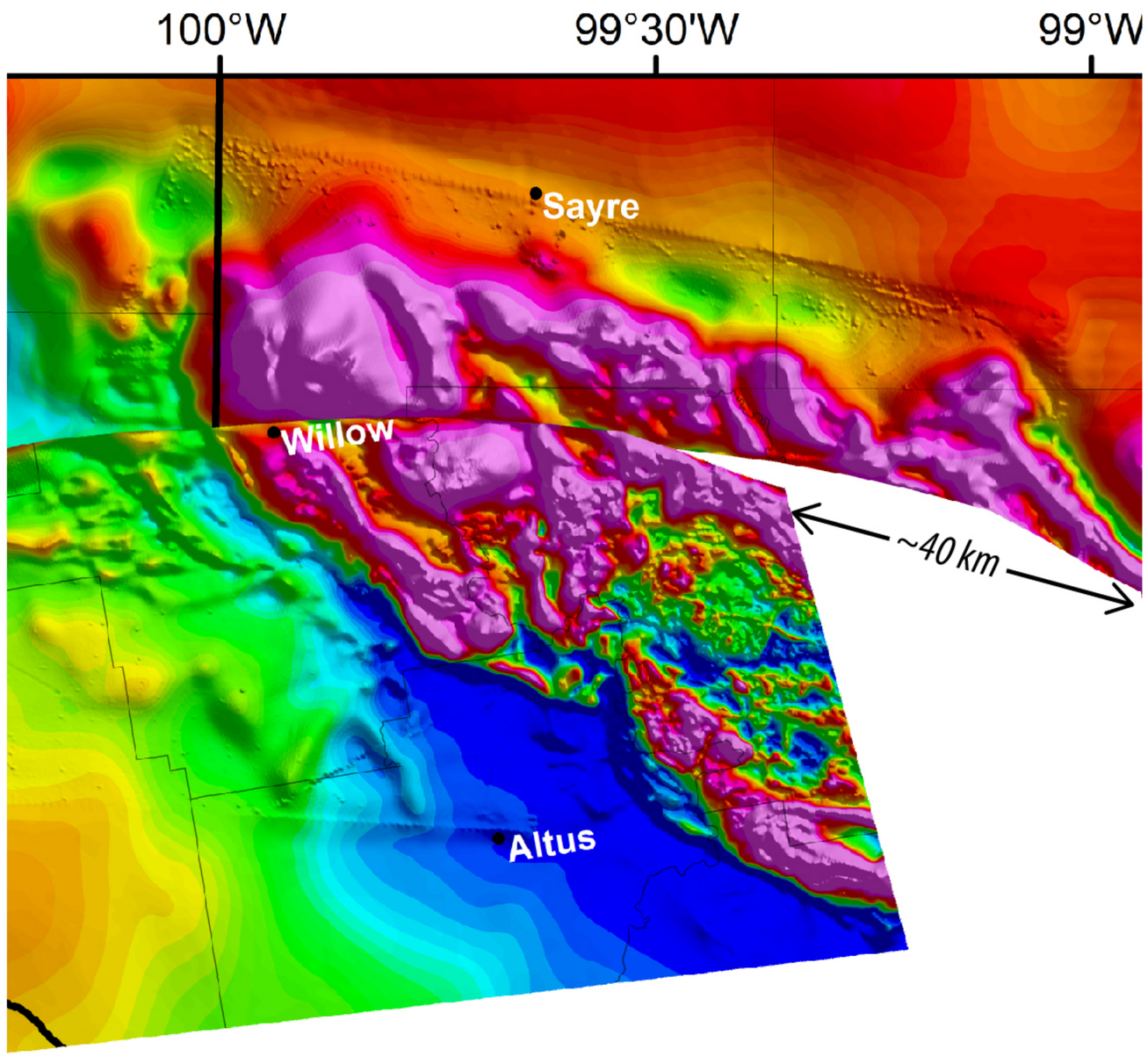
100°W
99°30'W
99°W
Sayre
Willow
~40 km
Altus

20 km

South

5 km

VE x2.3

North

Elevation (km)

0

-1

-2

-3

-4

-5

-6

-7

-8

-9

+

–

A

SL-1

SEI SEISMIC EXCHANGE

South

5 km

VE x3.5

North

Elevation (km)

0

-1

-2

-3

-4

-5

+

–

B

SL-2

SEI SEISMIC EXCHANGE